Heterojunction Transistors Printed via Instantaneous Oxidation of Liquid Metals

Andrew B. Hamlin[1], Simon A. Agnew[1], Justin C. Bonner[2], Julia W.P. Hsu[2], William J. Scheideler[1,]*

[1]Thayer School of Engineering, Dartmouth College, 15 Thayer Drive, Hanover, NH 03755, USA

[2]Department of Materials Science and Engineering, University of Texas at Dallas, 800 West Campbell Rd, Richardson, TX 75080, USA7

*Correspondence: william.j.scheideler@dartmouth.edu

ABSTRACT

Semiconducting transparent metal oxides are critical high mobility materials for flexible optoelectronic devices such as displays. We introduce the Continuous Liquid Metal Printing (CLMP) technique to enable rapid roll-to-roll compatible deposition of semiconducting two-dimensional (2D) metal oxide heterostructures. We leverage CLMP to deposit 10 cm^2-scale nanosheets of InO_x and GaO_x in seconds at a low process temperature ($T < 200$ ˚C) in air, fabricating heterojunction thin film transistors with 100X greater I_{on}/I_{off}, 4X steeper subthreshold slope, and a 50% increase in mobility over pure InO_x channels. Detailed nanoscale characterization of the heterointerface by XPS, UV-Vis, and KP elucidates the origins of enhanced electronic transport in these 2D heterojunctions. This combination of CLMP with the electrostatic control induced by the heterostructure architecture leads to high performance (μ_{lin} up to 22.6 cm^2/Vs) while reducing the process time for metal oxide transistors by greater than 100X compared with sol-gels and vacuum deposition methods.

KEYWORDS

2D semiconducting oxides, liquid metal printing, printed transistors, 2D heterostructures

Semiconducting metal oxides are critical materials for pushing the technological limits of emerging optoelectronic technologies such as flexible lightweight displays, transparent circuits, photodetector arrays, and gas sensors.[1–5] InO_x possesses a wide band gap and a high electron mobility, resulting in a highly conductive transparent channel material with a low number of thermally activated carriers.[6] Alloying with zinc and gallium can also transform degenerate InO_x into an amorphous channel material for fabricating stable, enhancement mode thin film transistors (TFTs).[7,8] The excellent bias-stress stability and mobility (> 10 cm^2/Vs) of quaternary metal oxides such as IGZO has led to their integration in fast switching OLED flat panel displays.[2,7–9] The semiconducting properties of oxide semiconductors such as InO_x can also be electrostatically controlled by reducing the channel thickness, as quantum confinement effects widen the bandgap and reduce the free carrier concentration.[6,10] These tunable electronic characteristics, in combination with the improved strain tolerance that ultrathin films exhibit, make InO_x an excellent candidate for flexible metal oxide-based electronics.[9,11,12]

Vacuum based processes such as sputtering and atomic layer deposition (ALD) are the current industry standard for the deposition of metal oxide channel materials such as InO_x.[2,3,13] However, sputtering and ALD require high capital expenditures, have lower material utilization, and present limitations for areal uniformity and substrate size. Solution processing InO_x is compatible with printing processes, is a relatively low cost means of manufacturing, and can yield high mobility, ultrathin films.[14–16] Unfortunately, a tradeoff exists between performance and thermal budget, as higher annealing temperatures are required to remove residual solvent contaminants and defects.[14,17] Liquid metal printing is an emerging vacuum-free, solvent-free, scalable method that offers the ability to deposit crystalline films in-air at low temperatures (< 200 ˚C).[10,11,18] This method operates based on Cabrera-Mott oxidation, which is responsible for the formation of an oxide skin on the surface of liquid metal, which can readily be adhered to a target substrate via van der Waals adhesive forces.[11] Previously, we printed large area, 2D nanosheets that can be rapidly fabricated via continuous rolling deposition, making this approach a breakthrough in the scalable production of metal oxide semiconductors.[18] Since the introduction of liquid metal surface oxide synthesis by Zavabeti *et al.* in 2017, In_2O_3, HfO_2, Al_2O_3, Ga_2O_3, SnO, TeO_2, ITO, IAO and IZO have been demonstrated via liquid metal printing to fabricate TFTs, UV photodetectors, gas sensors, inverters, amplifiers, dielectrics, and touch capacitive sensors.[4,11,13,18–22]

Recent reports of ultrathin channel TFTs demonstrate the importance of the passivation of the backchannel for achieving high mobility and good operational stability.[23–25] Heterostructure channels integrating layers with dissimilar work functions can also result in band bending due to Fermi level pinning at the heterointerface.[24] This phenomenon, referred to as modulation doping,[18,24,26] has been utilized to increase the carrier concentration in heterojunctions between InO_x, SnO_x, ZnO_x, AlO_x and GaO_x.[15,16,18,24–26] In our recent work (Ye *et al.*), we applied this effect to increase carrier concentration (>10^{20} cm^{-3}) and conductivity (>600 S/cm) through the fabrication of a layered InO_x / GaO_x superlattice using continuous liquid metal printing (CLMP).[18] However, the electrostatic control offered by these heterointerfaces can also be utilized for improving InO_x TFT performance through enhancement of the free carrier concentration, as shown previously for InO_x / ZnO_x heterojunctions.[15,24] A remaining challenge for heterostructure TFTs is capturing the advantages of higher mobility while controlling the turn on (V_{on}) voltage towards the goal of enhancement mode operation. Achieving this requires the precise nanoscale thickness and electronic transport control that 2D oxides provide, which has previously been challenging with sputtering and solution-processing.[10]

Herein, we present rapid CLMP of 2D InO_x and InO_x / GaO_x heterostructure TFTs in air in less than 6 seconds, using a maximum temperature of 200 ˚C. Devices were fabricated and measured with no additional post-deposition annealing. Passivation of the InO_x backchannel by GaO_x deposition is demonstrated to yield vastly improved switching characteristics such as a 3x improvement in subthreshold slope (SS), reduced off current and enhancement mode operation. We explore the use of a rapid in-air plasma treatment to modify the electronic properties of this heterostructure. The addition of surface plasma treatment to the heterointerface is shown to yield a modulation doping effect, as indicated by Burstein-Moss band gap widening of the optical band gap, a 50% increase in mobility, a negative shift in V_{on}, and an increased binding energy position of the In-3*d* core XPS peak position. This work highlights the impressive processing advantages of the CLMP process and demonstrates the resultant high-performance heterojunction bilayer channels for next-generation TFTs.

Figure 1 shows facile deposition of ultrathin metal oxide nanosheets using our roller-based printing technique. In Figure 1a, the substrate is plasma-treated to remove organic contaminants and to promote adhesive bonding between the surface and metal oxide. The desired metal is placed on the surface of the substrate, where it melts spontaneously, given that the substrate temperature is greater than the melting temperature of the metal. Figure 1b demonstrates the *continuous* deposition of an ultrathin metal oxide film, which has no inherent length limitation due to the millisecond scale regenerative Cabrera-Mott surface oxidization of the liquid metal that is being pushed in front of the roller. This method of oxide deposition makes this process a potentially high-impact, roll-to-roll compatible semiconductor technique. The final step is shown in Figure 1c, where microscale metal inclusions are easily removed using a silicone wiper. Additional details regarding CLMP deposition can be found in the experimental methods section of the SI.

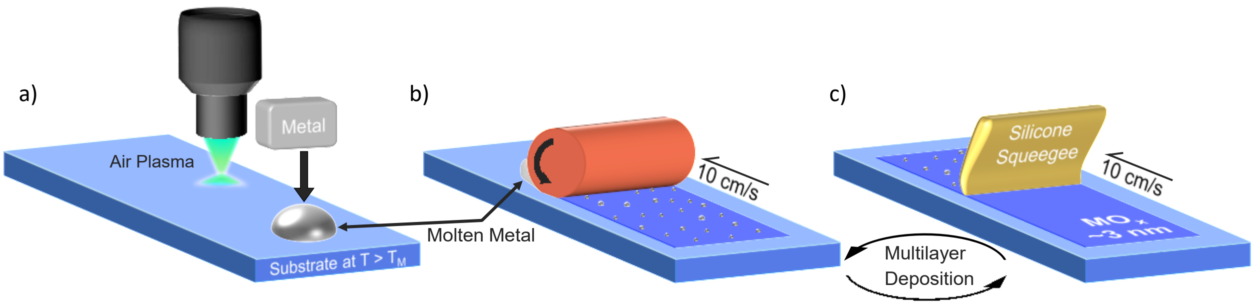

Figure 1. A schematic of the Continuous Liquid Metal Printing process showing (a) the surface cleaning and metal melting, (b) roller-based metal oxide deposition, and (c) metallic inclusion removal.

Figure 2 presents data collected from InO_x and InO_x / GaO_x heterostructure films with no interfacial treatment between the InO_x and GaO_x layers. XRD of these CLMP films show that they exhibit the InO_x cubic bixbyite structure for both pure InO_x and heterostructure InO_x / GaO_x films as shown in Figure 2a. No GaO_x peaks were detected, indicating the amorphous nature of this layer. The crystalline structure of these 2D films as deposited at 200 ˚C with no thermal annealing is unique to the liquid metal printing method.[10] Figure S1 presents the fitted curves to the InO_x (222) and (400) peaks. The peak widths, intensities and positions are similar for both InO_x and heterostructure films, indicating that the deposition of GaO_x has no effect on the crystallinity or texture of the InO_x layer beneath it. Given that the entire deposition procedure for these films is completed on the order of seconds, conservation of the InO_x crystalline structure during GaO_x deposition is unsurprising.

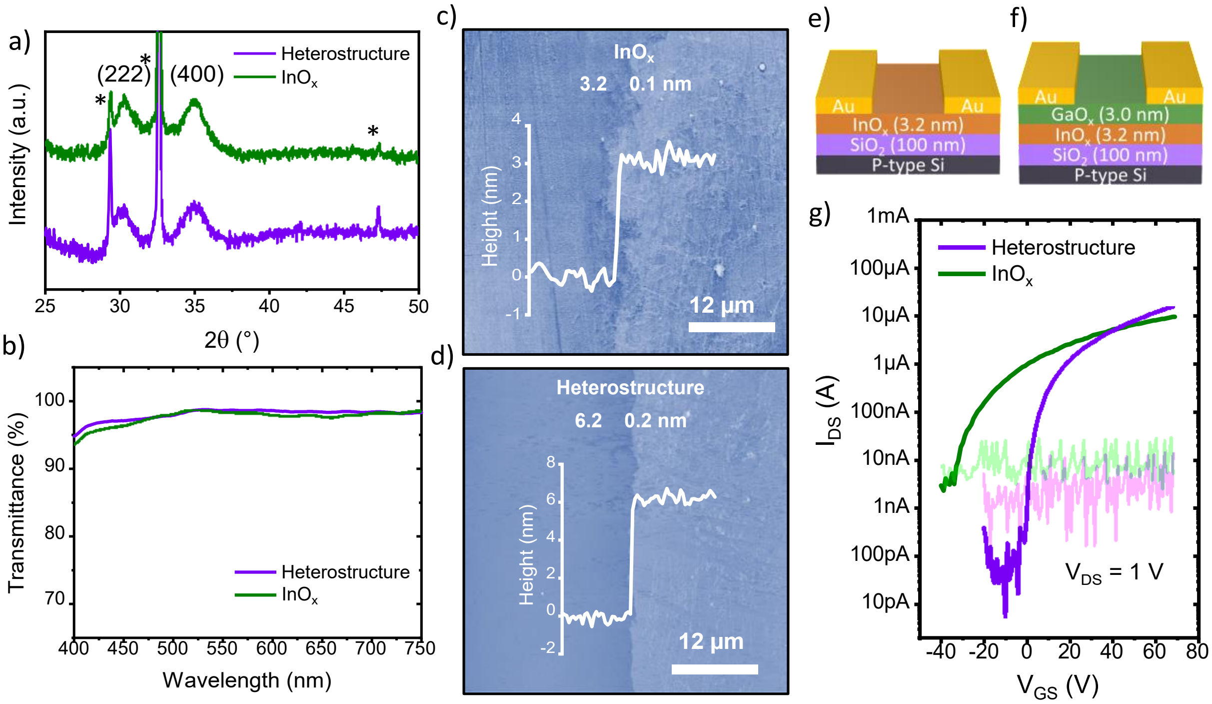

Figure 2. (a) XRD (* indicates a substrate peak), (b) transmittance, and (c-d) large area AFM characterization of CLMP InO_x and InO_x / GaO_x heterostructures. (e-f) TFT device architecture schematics of InO_x and heterojunction devices and (g) a representative transfer characteristic comparison with respective I_{gs} curves faded.

Figure 2b show the ultrahigh transmittance of InO_x and heterostructure films. With an average transmittance in the visible range of greater than 98%, these films are highly compatible with transparent electronic applications. The high transmittance is generally owed to the wide band gaps of InO_x and GaO_x. Their 2D nature also bolsters the transmittance of these thin films. Large area AFM scans in Figures 2c and 2d reveal a step height of 3.2 nm for CLMP InO_x, 6.2 nm for heterostructure films, and the uniformity that the printing process delivers. Figure S2 shows the surface roughness of 0.1 nm on the top of the InO_x layer, which aids the in fabrication of a smooth InO_x / GaO_x interface.

These films were integrated into bottom gate TFT devices with single layer and heterostructure channel architectures shown in Figures 2e and 2f, respectively. Figure S3 shows the XPS survey scan of heterostructure films, which confirms the presence of a GaO_x layer on top of the InO_x. Figure 2g shows the transfer characteristics of representative InO_x and heterostructure devices, which possess approximately median statistical values of critical device parameters such as SS, V_{on}, I_{on}/I_{off} and mobility. A significant performance enhancement is realized with the heterostructure architecture. A notably improved SS, off-current and positive shift in the turn on voltage are displayed. Interestingly, the shift in turn on voltage and difference in subthreshold slope can be corroborated with the transmittance scans presented in Figure 2b. For $\lambda < 450$ nm, InO_x exhibits a slightly higher absorption than heterostructure stacks.

To elucidate the consistency of the CLMP printing process, extensive characterization of batches of InO_x and heterostructure TFTs are presented in Table 1, where N=20 for all entries.

Table 1. Transistor performance summary for InO_x, heterostructure and heterostructure with plasma CLMP transistors

Channel	**SS (mV/dec)**	**V_{on} (V) (Linear)**	**$\log_{10}(I_{on}/I_{off})$**	**μ_0 (cm^2/Vs)**
InO_x	1000 ± 310	-35 ± 7.5	5.2 ± 0.5	12.3 ± 4.6
Heterostructure	230 ± 80	-2.3 ± 3.0	7.0 ± 0.4	13.5 ± 5.0
Heterostructure w/ Plasma	1020 ± 290	-36 ± 8.6	5.8 ± 0.5	17.5 ± 2.9

Transfer curves demonstrating inter-device repeatability for InOx and heterostructure devices are presented in Figure S4. The subthreshold slope is improved by more than 4X with the addition of a GaO_x backchannel layer. The devices also shift from depletion mode operation to enhancement mode operation, increasing their utility in circuit-level applications. Furthermore, the on-off ratio is augmented by nearly two orders of magnitude, which stems from a reduction in the off-current as shown in Figure 2f, revealing the improved efficiency of these devices in low power applications. The sole difference in the processing and production of these InO_x and heterostructure devices is the addition of the GaO_x capping layer, further indicating that the explanation for their improvement is passivation of the InO_x backchannel defects. Given the ultrathin dimensions of these films (3 nm), a strong dependence of the electronic TFT behavior on the InO_x back-channel surface states is expected. The GaO_x passivation is also demonstrated to reduce the degree of variation of the SS and V_{on} within the devices, which is explicitly presented in the form of histograms in Figure S5. A small improvement in mobility is also realized for these devices, which could correspond to the reduction in defects at the back-channel.

To further probe the physical properties of the InO_x / GaO_x heterojunction, a rapid 2 s in-air plasma treatment of the InO_x backchannel was applied before the deposition of the GaO_x

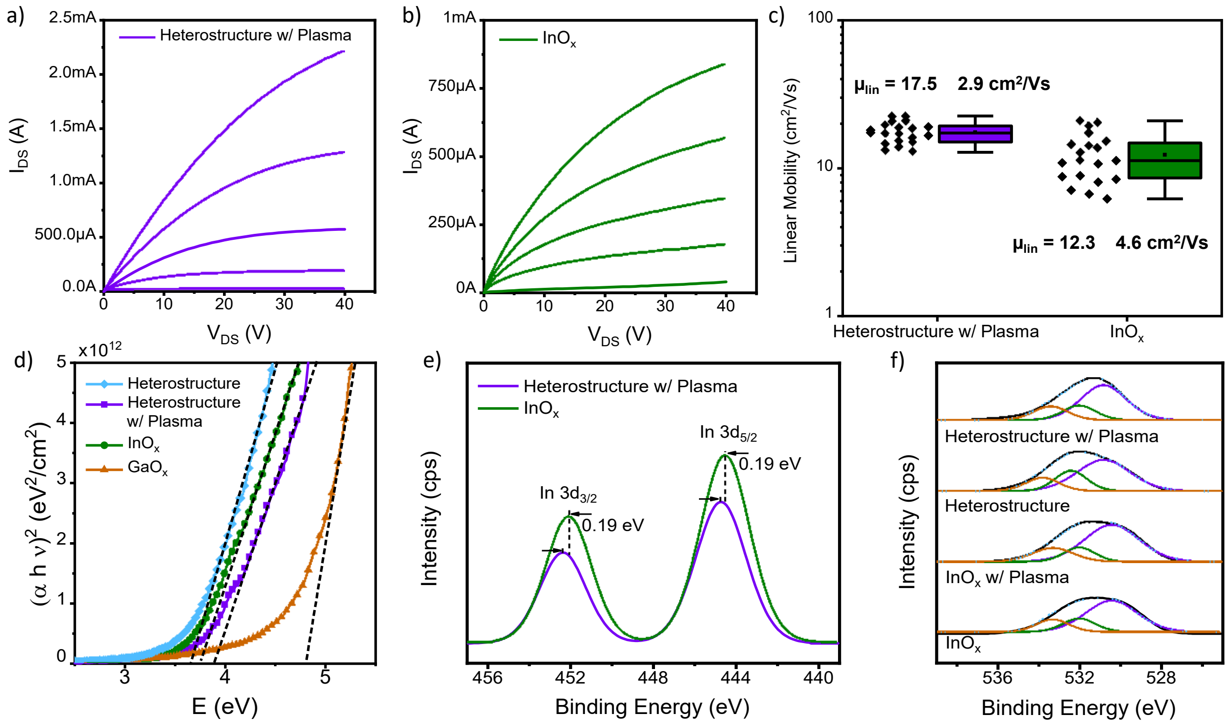

Figure 3. Output curves of (a) plasma-treated heterostructure and (b) InO_x devices scanned from V_{GS} = -40 V to 20 V in 15 V steps. (c) Batch mobility comparison of CLMP TFTs, where N = 20. (d) Tauc plots demonstrating optical E_g extraction from UV-Vis measurements. XPS characterization and deconvolution of (e) In-3*d* and (f) O-1*s* peaks for InO_x/GaO_x heterostructures and pure InO_x. In the O-1s peak deconvolution, purple corresponds to stoichiometric M-O bonding, green to oxygen deficient M-O bonding, and orange to M-OH bonding.

capping layer to create the samples and devices characterized in Figure 3 and row 3 of Table 1. Figure S6 clarifies the processing of the heterostructures and plasma-treated heterostructures. Figures 3a and 3b show the TFT output of plasma-treated heterostructures and pure InO_x devices, respectively. The heterostructure devices demonstrate a 3X increase in the output current. Figure S7 displays the transfer characteristic of heterostructure w/ plasma and pure InO_x devices, where a comparable trend is observed. The transfer characteristic displays the similar turn on potential of these two device architectures, showing the tuning effect towards depletion mode operation of plasma-treated InO_x / GaO_x heterostructure devices. Figure S7 also provides representative transfer characteristics of heterostructures without plasma, and pure InO_x devices with backchannel plasma exposure but no GaO_x capping layer. The backchannel plasma is shown to decrease the on current of pure InO_x device and induce a slight positive shift in the V_{on}.

Figure 3c presents a batch mobility characterization of TFTs with heterostructure channels treated with plasma vs. TFTs with single layer InO_x channels. The addition of the GaO_x layer provides a mobility enhancement of 50 %, leading to a high average μ_{lin} of 17.5 ± 2.9 cm^2/Vs as well as a significant reduction in device variability. Here, the coefficient of variation (CV) is reduced by 2.3X for heterostructure devices. To uncover the origin of the improvement in mobility for these structures, the optical band gap energy was extracted via a direct bandgap Tauc plot fit (Figure 3d) from UV-Vis absorption measurements (S8). An increase in the optical band gap for heterostructures treated with plasma (InO_x / GaO_x) compared with pure InO_x is revealed, indicating a Burstein-Moss shift in the InO_x that is consistent with a higher free carrier concentration. A slight decrease in the optical band gap without the use of plasma at the InO_x / GaO_x interface is observed.

The XPS signals for InO_x and InO_x / GaO_x heterostructure films reveal details of the composition and electronic structure of these materials. Figure 3e shows the In-3$d_{5/2}$ and In-3$d_{3/2}$ peaks located at 444.6 and 452.1 eV, respectively. Plasma-treated heterostructure films display a positive shift of 0.2 eV for the binding energy of the heterostructures, which indicates an increase

Table 2. Summary of XPS peak fitting results of InO_x and heterostructure channel materials

Material	M-O (Stoichiometric) (%)	M-O (O Deficient) (%)	M-OH (%)
InO_x	66	18	17
Heterostructure	60	23	16
InO_x w/ Plasma	67	15	19
Heterostructure w/ Plasma	62	19	19

in the Fermi level in these samples. This binding energy shift is often correlated with an increase in carrier concentration as a result of modulation doping.[15,17,24,26] To further examine chemical and electronic structure, the O1*s* peak is deconvolved in Figure 3f. The peak is broken down into stoichiometric metal-oxygen (M-O) bonding (530 eV), oxygen deficient substoichiometric (M-O) bonding (531 eV), and metal-hydroxide (M-OH) bonding (532 eV). A summary of the results of this deconvolution is presented in Table 2. To target the film composition instead of the substrate signal, the InO_x films utilized for this measurement are two layers thick. In the case of heterostructures, a measured signal is expected to be received from both the GaO_x and InO_x layers.

CLMP InO_x is dominated by stoichiometric M-O bonding, whereas heterostructures possess a higher percentage of oxygen deficient M-O bonding, indicating that the GaO_x layer is more oxygen deficient than InO_x. Based on previous results such as the improved on current and shift in the In-3*d*, we expect that the defective GaO_x is responsible for the observed electronic enhancement.[18] We also note that plasma-treated samples possess a higher concentration of M-OH bonding, which is the case for both pure InO_x and heterostructure films. The in-air plasma jet used in this study is known to entrain water vapor from the atmosphere and has been observed to generate OH radicals[27], which could be responsible for our observations of the hydroxide content of these films.

Table 3. Summary of experimentally measured work function, PESA defect ionization energy, and optical band gap of InO_x and GaO_x films and their heterostructures

Material	Work Function (eV)	PESA Defect Ionization Energy (eV)	Optical Band Gap (eV)
Heterostructure	4.34 ± .01	4.85 ± .05	3.69 ± .03
Heterostructure w/ Plasma	4.11 ± .01	4.53 ± .05	3.82 ± .03
InO_x	4.30 ± .01	4.75 ± .05	3.73 ± .03
GaO_x	4.11 ± .01	4.57 ± .05	4.87 ± .03

Table 3 presents the work functions (WF), PESA defect ionization energies (IE) and optical band gaps of InO_x, GaO_x, InO_x / GaO_x heterostructures, and interlayer plasma-treated InO_x / GaO_x heterostructures as acquired by Kelvin probe (KP) measurements, photoelectron spectroscopy in air (PESA) (Figure S9) and UV-Vis[28,29], respectively. Row 1 shows that the InO_x / GaO_x heterostructure exhibits a similar but slightly larger WF and defect IE, and a similar E_g when compared to pure InO_x. The PESA defect IE measurements are expected to correspond to subgap defect levels, as has been observed in other works.[30] This observation is consistent with the transfer characteristics shown in Figure 2g, where the subthreshold slope is improved and turn on voltage is shifted positively. One explanation for these results is that, in this case of the heterostructure, the GaO_x effectively passivates InO_x backchannel defects. These defect states may otherwise play an important role in increasing the subthreshold slope and decreasing the V_{on}.

Row 2 of Table 3 shows that the addition of plasma treatment to the InO_x / GaO_x interface leads to a significantly lower WF (-0.23 eV) and defect IE (-0.32 eV), corresponding to a higher

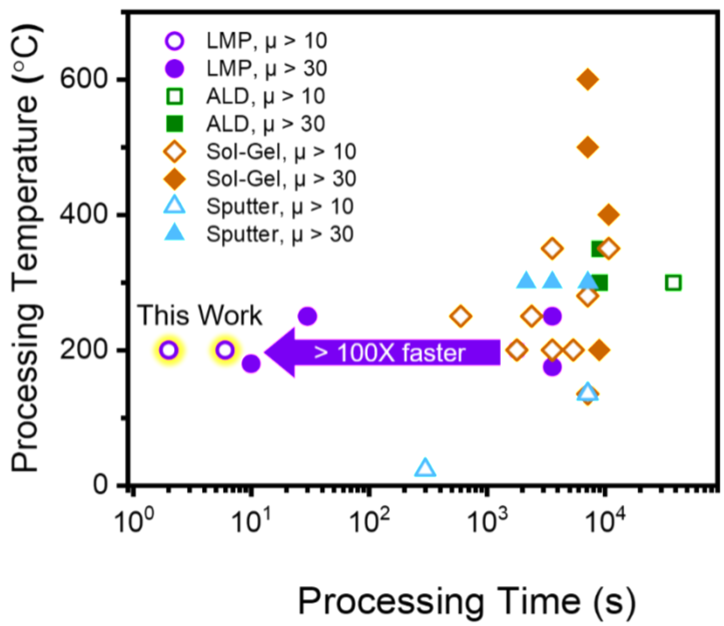

Figure 4. A comparison of processing temperature, processing time and mobility for InO_x thin film transistors fabricated by multiple deposition methods including sputtering, sol-gel processing, ALD, and liquid metal printing. μ refers to the linear field effect mobility with units of cm^2/Vs.

Fermi level in the InO_x and thus, a larger free electron concentration. This result is consistent with the higher output current shown in the I-V characteristics in Figures 3a-3b and the increase in optical band gap energy shown by UV-Vis absorption. Rows 3 and 4 show that the WF and defect IE of GaO_x are ~0.2 eV smaller than that of InO_x. Since GaO_x has a smaller work function than InO_x, when these two materials are put in contact, the heterointerface has the potential to produce a modulation doping effect.[26] Our hypothesis is that interlayer plasma treatment between InO_x and GaO_x facilitates the modulation doping effect in this heterostructure. Recent observations by HRTEM of a van der Waals gap between layers of 2D oxides[11] could suggest one possible mechanism to explain effective modulation doping at the plasma-treated InO_x / GaO_x interface.

To put the results of this study in context as a scheme for rapid fabrication of high mobility transistors, Figure 4 highlights the processing time, temperature and resulting TFT mobility of liquid metal printing compared with ALD, sol-gel processing, and sputtering.[10,13–18,22,25,31–43] LMP is compatible with ultra-rapid processing times (< 6 seconds) when compared to the other three methods, but offers the ability to form high mobility (μ_{eff} > 10 cm^2/Vs) channels comparable to vacuum-deposition. Sol-gels require high temperatures and 100-1000x longer times than CLMP to drive elimination and condensation reactions to completion. Without sufficient annealing, contaminants such as carbonaceous impurities and precursor residues such as nitrogen and chlorine detract from their performance. Typically, a temperature of 250 ˚C or higher is required to complete this transition and achieve high performance sol-gel oxide TFTs.[44] Sputtering offers low temperature processing capability, but due to the fact that is a vacuum process, a post anneal is often necessary to induce crystallization and adjust stoichiometry to yield the desired electrical characteristics for thin film transistors. ALD can match the ultrathin thickness that LMP films possess but has drawbacks when it comes to processing time and temperature. ALD's cyclic growth is inherently limited by chamber purge times, and high temperatures are required to fully decompose precursors and eliminate residual carbon. Similar to sputtering, a thermal anneal is often utilized to achieve a crystalline film with the desired stoichiometry. Ultimately, the combination of low-temperatures and rapid processing can allow LMP to become a breakthrough technology for inorganic electronics in terms of reducing semiconductor fabrication time and improving compatibility with flexible substrates.

To the best of our knowledge, this work is the first report of 2D oxide heterostructures for switching devices. We demonstrate the utility of our novel CLMP metal oxide fabrication technique to yield high performance electronic devices. These 2D films are rapidly printed in air, at low temperatures, and do not require any post-deposition treatment to be integrated into high mobility TFTs. We demonstrate the synergy of an InO_x / GaO_x backchannel interface by achieving low subthreshold slope, enhancement mode devices with high on-off ratios. Our characterization of the heterointerface by KP, XPS, and UV-Vis points to the finding that the GaO_x passivation layer could reduce the number of surface defects on the InO_x backchannel. Furthermore, the tunability of this interface is operated via a rapid in-air plasma treatment to also achieve depletion mode TFTs with a mobility improvement of ~50%. We demonstrate the enhancement of InO_x through GaO_x modulation doping, which is supported by UV-Vis, I-V measurements, and XPS. The work presented in this study is one of the most rapid, low-cost and low thermal budget productions of InO_x TFTs to date, establishing CLMP as a promising commercial approach to flexible electronics and flat-panel display fabrication.

ASSOCIATED CONTENT

Supporting Information

The supporting information contains details about the experimental methodology, XRD of InO_x and heterostructure films, surface roughness AFM of InO_x, XPS of GaO_x peaks for heterostructure films, comparative performance histograms of InO_x and heterostructure TFTs and a representative transfer characteristic of a plasma-treated heterostructure TFT (PDF).

AUTHOR INFORMATION

Corresponding Author

William J. Scheideler- *Thayer School of Engineering, Dartmouth College, 15 Thayer Drive, Hanover, NH 03755, United States*; Email: william.j.scheideler@dartmouth.edu

Authors

Andrew B. Hamlin- *Thayer School of Engineering, Dartmouth College, 15 Thayer Drive, Hanover, NH 03755, United States*

Simon A. Agnew- *Thayer School of Engineering, Dartmouth College, 15 Thayer Drive, Hanover, NH 03755, United States*

Justin C. Bonner- *Department of Materials Science and Engineering, University of Texas at Dallas, 800 West Campbell Rd, Richardson, TX 75080, United States*

Julia W.P. Hsu- *Department of Materials Science and Engineering, University of Texas at Dallas, 800 West Campbell Rd, Richardson, TX 75080, United States*

Author Contributions

The manuscript was written through contributions of all authors. All authors have given approval to the final version of the manuscript. ABH and WJS conceived of the project. WJS supervised the project and edited the manuscript. ABH fabricated the films and devices, performed the measurements, and wrote the manuscript. SAA executed the literature review comparison. JCB ran the KP experiments and performed the analysis. JWPH secured the funding for work done at UTD and edited the manuscript.

Funding Sources

ABH is supported by the NSF Graduate Research Fellowship Program. This research was supported by the National Science Foundation Electronic and Photonic Materials program (Award #2202501) as well as the National Science Foundation Electronics, Photonics, and Magnetic Devices program (Award #2219991). JCB is supported by the U.S. Department of Energy's Office of Energy Efficiency and Renewable Energy (EERE) under the Solar Energy Technologies Office Award Number DE-EE0009518. JWPH acknowledges partial support of Texas Instruments Distinguished Chair in Nanoelectronics.

Notes

The authors declare no competing financial interest.

Full Legal Disclaimer: This report was prepared as an account of work sponsored by an agency of the United States Government. Neither the United States Government nor any agency thereof, nor any of their employees, makes any warranty, express or implied, or assumes any legal liability or responsibility for the accuracy, completeness, or usefulness of any information, apparatus, product, or process disclosed, or represents that its use would not infringe privately owned rights.

Reference herein to any specific commercial product, process, or service by trade name, trademark, manufacturer, or otherwise does not necessarily constitute or imply its endorsement, recommendation, or favoring by the United States Government or any agency thereof. The views and opinions of authors expressed herein do not necessarily state or reflect those of the United States Government or any agency thereof.

ACKNOWLEDGMENT

We acknowledge John Wilderman at UNH for taking the XPS measurements.

ABBREVIATIONS

CLMP, continuous liquid metal printing; V_{on}, turn on voltage; 2D, 2-dimensional; TFT, thin film transistor; IGZO, indium-gallium-zinc oxide; ALD, atomic-layer deposition; SS, subthreshold slope; CV, coefficient of variation; M-O, Metal-Oxygen; M-OH, Metal-Hydroxide; WF, work function; IE, ionization energy, KP, Kelvin probe; PESA, photoelectron-spectroscopy in air.

REFERENCES

(1) Shankar, U.; Oberoi, D.; Bandyopadhyay, A. A Review on the Alternative of Indium Tin Oxide Coated Glass Substrate in Flexible and Bendable Organic Optoelectronic Device. *Polym. Adv. Technol.* **2022**, *33* (10), 3078–3111. https://doi.org/10.1002/pat.5797.
(2) Hara, Y.; Kikuchi, T.; Kitagawa, H.; Morinaga, J.; Ohgami, H.; Imai, H.; Daitoh, T.; Matsuo, T. IGZO-TFT Technology for Large-Screen 8K Display. *J. Soc. Inf. Disp.* **2018**, *26* (3), 169–177. https://doi.org/10.1002/jsid.648.
(3) Han, C.-W.; Kim, K.-M.; Bae, S.-J.; Choi, H.-S.; Lee, J.-M.; Kim, T.-S.; Tak, Y.-H.; Cha, S.-Y.; Ahn, B.-C. 21.2: 55-Inch FHD OLED TV Employing New Tandem WOLEDs. *SID Symp. Dig. Tech. Pap.* **2012**, *43* (1), 279–281. https://doi.org/10.1002/j.2168-0159.2012.tb05768.x.
(4) Li, Q.; Lin, J.; Liu, T.-Y.; Zhu, X.-Y.; Yao, W.-H.; Liu, J. Gas-Mediated Liquid Metal Printing toward Large-Scale 2D Semiconductors and Ultraviolet Photodetector. *Npj 2D Mater. Appl.* **2021**, *5* (1), 36. https://doi.org/10.1038/s41699-021-00219-y.
(5) Vijjapu, M. T.; Surya, S. G.; Yuvaraja, S.; Zhang, X.; Alshareef, H. N.; Salama, K. N. Fully Integrated Indium Gallium Zinc Oxide NO2 Gas Detector. *ACS Sens.* **2020**, *5* (4), 984–993. https://doi.org/10.1021/acssensors.9b02318.
(6) Si, M.; Hu, Y.; Lin, Z.; Sun, X.; Charnas, A.; Zheng, D.; Lyu, X.; Wang, H.; Cho, K.; Ye, P. D. Why In2O3 Can Make 0.7 Nm Atomic Layer Thin Transistors. *Nano Lett.* **2021**, *21* (1), 500–506. https://doi.org/10.1021/acs.nanolett.0c03967.

(7) Hoshino, K.; Hong, D.; Chiang, H. Q.; Wager, J. F. Constant-Voltage-Bias Stress Testing of a-IGZO Thin-Film Transistors. *IEEE Trans. Electron Devices* **2009**, *56* (7), 1365–1370. https://doi.org/10.1109/TED.2009.2021339.
(8) Peng, C.; Yang, S.; Pan, C.; Li, X.; Zhang, J. Effect of Two-Step Annealing on High Stability of a-IGZO Thin-Film Transistor. *IEEE Trans. Electron Devices* **2020**, *67* (10), 4262–4268. https://doi.org/10.1109/TED.2020.3017718.
(9) Sheng, J.; Hong, T.; Lee, H.-M.; Kim, K.; Sasase, M.; Kim, J.; Hosono, H.; Park, J.-S. Amorphous IGZO TFT with High Mobility of ∼70 Cm^2 /(V s) via Vertical Dimension Control Using PEALD. *ACS Appl. Mater. Interfaces* **2019**, *11* (43), 40300–40309. https://doi.org/10.1021/acsami.9b14310.
(10) Hamlin, A. B.; Ye, Y.; Huddy, J. E.; Rahman, M. S.; Scheideler, W. J. 2D Transistors Rapidly Printed from the Crystalline Oxide Skin of Molten Indium. *Npj 2D Mater. Appl.* **2022**, *6* (1), 16. https://doi.org/10.1038/s41699-022-00294-9.
(11) Datta, R. S.; Syed, N.; Zavabeti, A.; Jannat, A.; Mohiuddin, M.; Rokunuzzaman, M.; Yue Zhang, B.; Rahman, M. A.; Atkin, P.; Messalea, K. A.; Ghasemian, M. B.; Gaspera, E. D.; Bhattacharyya, S.; Fuhrer, M. S.; Russo, S. P.; McConville, C. F.; Esrafilzadeh, D.; Kalantar-Zadeh, K.; Daeneke, T. Flexible Two-Dimensional Indium Tin Oxide Fabricated Using a Liquid Metal Printing Technique. *Nat. Electron.* **2020**, *3* (1), 51–58. https://doi.org/10.1038/s41928-019-0353-8.
(12) Nomura, K.; Ohta, H.; Takagi, A.; Kamiya, T.; Hirano, M.; Hosono, H. Room-Temperature Fabrication of Transparent Flexible Thin-Film Transistors Using Amorphous Oxide Semiconductors. *Nature* **2004**, *432* (7016), 488–492. https://doi.org/10.1038/nature03090.
(13) Tang, Y.; Huang, C.-H.; Nomura, K. Vacuum-Free Liquid-Metal-Printed 2D Indium–Tin Oxide Thin-Film Transistor for Oxide Inverters. *ACS Nano* **2022**, *16* (2), 3280–3289. https://doi.org/10.1021/acsnano.1c11205.
(14) Faber, H.; Lin, Y.-H.; Thomas, S. R.; Zhao, K.; Pliatsikas, N.; McLachlan, M. A.; Amassian, A.; Patsalas, P. A.; Anthopoulos, T. D. Indium Oxide Thin-Film Transistors Processed at Low Temperature via Ultrasonic Spray Pyrolysis. *ACS Appl. Mater. Interfaces* **2015**, *7* (1), 782–790. https://doi.org/10.1021/am5072139.
(15) Faber, H.; Das, S.; Lin, Y.-H.; Pliatsikas, N.; Zhao, K.; Kehagias, T.; Dimitrakopulos, G.; Amassian, A.; Patsalas, P. A.; Anthopoulos, T. D. Heterojunction Oxide Thin-Film Transistors with Unprecedented Electron Mobility Grown from Solution. *Sci. Adv.* **2017**. https://doi.org/10.1126/sciadv.1602640.
(16) Lin, Y.-H.; Faber, H.; Labram, J. G.; Stratakis, E.; Sygellou, L.; Kymakis, E.; Hastas, N. A.; Li, R.; Zhao, K.; Amassian, A.; Treat, N. D.; McLachlan, M.; Anthopoulos, T. D. High Electron Mobility Thin-Film Transistors Based on Solution-Processed Semiconducting Metal Oxide Heterojunctions and Quasi-Superlattices. *Adv. Sci.* **2015**, *2* (7), 1500058. https://doi.org/10.1002/advs.201500058.
(17) Tetzner, K.; Isakov, I.; Regoutz, A.; Payne, D. J.; Anthopoulos, T. D. The Impact of Post-Deposition Annealing on the Performance of Solution-Processed Single Layer In_2O_3 and Isotype In_2O_3/ZnO Heterojunction Transistors. *J. Mater. Chem. C* **2017**, *5* (1), 59–64. https://doi.org/10.1039/C6TC04907A.
(18) Ye, Y.; Hamlin, A. B.; Huddy, J. E.; Rahman, M. S.; Scheideler, W. J. Continuous Liquid Metal Printed 2D Transparent Conductive Oxide Superlattices. *Adv. Funct. Mater.* **2022**, *32* (33), 2204235. https://doi.org/10.1002/adfm.202204235.

(19) Zavabeti, A.; Ou, J. Z.; Carey, B. J.; Syed, N.; Orrell-Trigg, R.; Mayes, E. L. H.; Xu, C.; Kavehei, O.; O'Mullane, A. P.; Kaner, R. B.; Kalantar-zadeh, K.; Daeneke, T. A Liquid Metal Reaction Environment for the Room-Temperature Synthesis of Atomically Thin Metal Oxides. *Science* **2017**, *358* (6361), 332–335. https://doi.org/10.1126/science.aao4249.
(20) Jannat, A.; Syed, N.; Xu, K.; Rahman, Md. A.; Talukder, Md. M. M.; Messalea, K. A.; Mohiuddin, Md.; Datta, R. S.; Khan, M. W.; Alkathiri, T.; Murdoch, B. J.; Reza, S. Z.; Li, J.; Daeneke, T.; Zavabeti, A.; Ou, J. Z. Printable Single-Unit-Cell-Thick Transparent Zinc-Doped Indium Oxides with Efficient Electron Transport Properties. *ACS Nano* **2021**, *15* (3), 4045–4053. https://doi.org/10.1021/acsnano.0c06791.
(21) Zavabeti, A.; Aukarasereenont, P.; Tuohey, H.; Syed, N.; Jannat, A.; Elbourne, A.; Messalea, K. A.; Zhang, B. Y.; Murdoch, B. J.; Partridge, J. G.; Wurdack, M.; Creedon, D. L.; van Embden, J.; Kalantar-Zadeh, K.; Russo, S. P.; McConville, C. F.; Daeneke, T. High-Mobility p-Type Semiconducting Two-Dimensional β-TeO2. *Nat. Electron.* **2021**, *4* (4), 277–283. https://doi.org/10.1038/s41928-021-00561-5.
(22) Nguyen, C. K.; Low, M. X.; Zavabeti, A.; Murdoch, B. J.; Guo, X.; Aukarasereenont, P.; Mazumder, A.; Dubey, A.; Jannat, A.; Rahman, Md. A.; Chiang, K.; Truong, V. K.; Bao, L.; McConville, C. F.; Walia, S.; Daeneke, T.; Syed, N. Atomically Thin Antimony-Doped Indium Oxide Nanosheets for Optoelectronics. *Adv. Opt. Mater. n/a* (n/a), 2200925. https://doi.org/10.1002/adom.202200925.
(23) Ding, Y.; Fan, C.; Fu, C.; Meng, Y.; Liu, G.; Shan, F. High-Performance Indium Oxide Thin-Film Transistors With Aluminum Oxide Passivation. *IEEE Electron Device Lett.* **2019**, *40* (12), 1949–1952. https://doi.org/10.1109/LED.2019.2947762.
(24) Khim, D.; Lin, Y.-H.; Nam, S.; Faber, H.; Tetzner, K.; Li, R.; Zhang, Q.; Li, J.; Zhang, X.; Anthopoulos, T. D. Modulation-Doped In2O3/ZnO Heterojunction Transistors Processed from Solution. *Adv. Mater.* **2017**, *29* (19), 1605837. https://doi.org/10.1002/adma.201605837.
(25) Krausmann, J.; Sanctis, S.; Engstler, J.; Luysberg, M.; Bruns, M.; Schneider, J. J. Charge Transport in Low-Temperature Processed Thin-Film Transistors Based on Indium Oxide/Zinc Oxide Heterostructures. *ACS Appl. Mater. Interfaces* **2018**, *10* (24), 20661–20671. https://doi.org/10.1021/acsami.8b03322.
(26) Weidner, M.; Fuchs, A.; Bayer, T. J. M.; Rachut, K.; Schnell, P.; Deyu, G. K.; Klein, A. Defect Modulation Doping. *Adv. Funct. Mater.* **2019**, *29* (14), 1807906. https://doi.org/10.1002/adfm.201807906.
(27) Yonemori, S.; Nakagawa, Y.; Ono, R.; Oda, T. Measurement of OH Density and Air–Helium Mixture Ratio in an Atmospheric-Pressure Helium Plasma Jet. *J. Phys. Appl. Phys.* **2012**, *45* (22), 225202. https://doi.org/10.1088/0022-3727/45/22/225202.
(28) Kronik, L.; Shapira, Y. Surface Photovoltage Phenomena: Theory, Experiment, and Applications. *Surf. Sci. Rep.* **1999**, *37* (1), 1–206. https://doi.org/10.1016/S0167-5729(99)00002-3.
(29) Lee, Y.-J.; Wang, J.; Hsu, J. W. P. Surface Photovoltage Characterization of Organic Photovoltaic Devices. *Appl. Phys. Lett.* **2013**, *103* (17), 173302. https://doi.org/10.1063/1.4827104.
(30) Marques, F. C.; Jasieniak, J. J. Ionization Potential and Electron Attenuation Length of Titanium Dioxide Deposited by Atomic Layer Deposition Determined by Photoelectron Spectroscopy in Air. *Appl. Surf. Sci.* **2017**, *422*, 504–508. https://doi.org/10.1016/j.apsusc.2017.06.062.

(31) Jaehnike, F.; Pham, D. V.; Anselmann, R.; Bock, C.; Kunze, U. High-Quality Solution-Processed Silicon Oxide Gate Dielectric Applied on Indium Oxide Based Thin-Film Transistors. *ACS Appl. Mater. Interfaces* **2015**, *7* (25), 14011–14017. https://doi.org/10.1021/acsami.5b03105.

(32) Han, S.-Y.; Herman, G. S.; Chang, C. Low-Temperature, High-Performance, Solution-Processed Indium Oxide Thin-Film Transistors. *J. Am. Chem. Soc.* **2011**, *133* (14), 5166–5169. https://doi.org/10.1021/ja104864j.

(33) Huang, W.; Zhu, B.; Chang, S.-Y.; Zhu, S.; Cheng, P.; Hsieh, Y.-T.; Meng, L.; Wang, R.; Wang, C.; Zhu, C.; McNeill, C.; Wang, M.; Yang, Y. High Mobility Indium Oxide Electron Transport Layer for an Efficient Charge Extraction and Optimized Nanomorphology in Organic Photovoltaics. *Nano Lett.* **2018**, *18* (9), 5805–5811. https://doi.org/10.1021/acs.nanolett.8b02452.

(34) Si, M.; Lin, Z.; Charnas, A.; Ye, P. D. Scaled Atomic-Layer-Deposited Indium Oxide Nanometer Transistors With Maximum Drain Current Exceeding 2 A/Mm at Drain Voltage of 0.7 V. *IEEE Electron Device Lett.* **2021**, *42* (2), 184–187. https://doi.org/10.1109/LED.2020.3043430.

(35) Lee, J.; Moon, J.; Pi, J.-E.; Ahn, S.-D.; Oh, H.; Kang, S.-Y.; Kwon, K.-H. High Mobility Ultra-Thin Crystalline Indium Oxide Thin Film Transistor Using Atomic Layer Deposition. *Appl. Phys. Lett.* **2018**, *113* (11), 112102. https://doi.org/10.1063/1.5041029.

(36) Yeom, H.-I.; B. Ko, J.; Mun, G.; Ko Park, S.-H. High Mobility Polycrystalline Indium Oxide Thin-Film Transistors by Means of Plasma-Enhanced Atomic Layer Deposition. *J. Mater. Chem. C* **2016**, *4* (28), 6873–6880. https://doi.org/10.1039/C6TC00580B.

(37) Ma, Q.; Zheng, H.-M.; Shao, Y.; Zhu, B.; Liu, W.-J.; Ding, S.-J.; Zhang, D. W. Atomic-Layer-Deposition of Indium Oxide Nano-Films for Thin-Film Transistors. *Nanoscale Res. Lett.* **2018**, *13* (1), 4. https://doi.org/10.1186/s11671-017-2414-0.

(38) Qijun, Y.; Dejie, L. Indium Oxide Thin Film Transistors via Reactive Sputtering Using Metal Targets. *Phys. Status Solidi A* **2008**, *205* (2), 389–391. https://doi.org/10.1002/pssa.200723462.

(39) Flewitt, A. J.; Dutson, J. D.; Beecher, P.; Paul, D.; Wakeham, S. J.; Vickers, M. E.; Ducati, C.; Speakman, S. P.; Milne, W. I.; Thwaites, M. J. Stability of Thin Film Transistors Incorporating a Zinc Oxide or Indium Zinc Oxide Channel Deposited by a High Rate Sputtering Process. *Semicond. Sci. Technol.* **2009**, *24* (8), 085002. https://doi.org/10.1088/0268-1242/24/8/085002.

(40) Noh, J. H.; Ryu, S. Y.; Jo, S. J.; Kim, C. S.; Sohn, S.-W.; Rack, P. D.; Kim, D.-J.; Baik, H. K. Indium Oxide Thin-Film Transistors Fabricated by RF Sputtering at Room Temperature. *IEEE Electron Device Lett.* **2010**, *31* (6), 567–569. https://doi.org/10.1109/LED.2010.2046133.

(41) Zhang, H. Z.; Cao, H. T.; Chen, A. H.; Liang, L. Y.; Liu, Z. M.; Wan, Q. Enhancement of Electrical Performance in In2O3 Thin-Film Transistors by Improving the Densification and Surface Morphology of Channel Layers. *Solid-State Electron.* **2010**, *54* (4), 479–483. https://doi.org/10.1016/j.sse.2009.12.025.

(42) Ebata, K.; Tomai, S.; Tsuruma, Y.; Iitsuka, T.; Matsuzaki, S.; Yano, K. High-Mobility Thin-Film Transistors with Polycrystalline In–Ga–O Channel Fabricated by DC Magnetron Sputtering. *Appl. Phys. Express* **2012**, *5* (1), 011102. https://doi.org/10.1143/APEX.5.011102.

(43) Magari, Y.; Kataoka, T.; Yeh, W.; Furuta, M. High-Mobility Hydrogenated Polycrystalline In2O3 (In2O3:H) Thin-Film Transistors. *Nat. Commun.* **2022**, *13* (1), 1078. https://doi.org/10.1038/s41467-022-28480-9.
(44) Chen, H.; Rim, Y. S.; Jiang, C.; Yang, Y. Low-Impurity High-Performance Solution-Processed Metal Oxide Semiconductors via a Facile Redox Reaction. *Chem. Mater.* **2015**, *27* (13), 4713–4718. https://doi.org/10.1021/acs.chemmater.5b01347.